



This is the accepted manuscript made available via CHORUS. The article has been published as:

XUV superfluorescence from helium gas in the paraxial three-dimensional approximation

Špela Krušič, Andrej Mihelič, Klemen Bučar, Andrei Benediktovitch, Stasis Chuchurka, and Matjaž Žitnik

Phys. Rev. A **107**, 013113 — Published 24 January 2023

DOI: [10.1103/PhysRevA.107.013113](https://doi.org/10.1103/PhysRevA.107.013113)

XUV superfluorescence from helium gas in the paraxial 3D approximation

Špela Krušič,^{1,2} Andrej Mihelič,¹ Klemen Bučar,¹ Andrei Benediktovitch,³ Stasis Chuchurka,³ and Matjaž Žitnik¹

¹*Jožef Stefan Institute, 1000 Ljubljana, Slovenia*

²*Faculty of Mathematics and Physics,*

University of Ljubljana, 1000 Ljubljana, Slovenia

³*Deutsches Elektronen-Synchrotron DESY, Hamburg 22607, Germany*

(Dated: December 23, 2022)

Abstract

We present the results of a theoretical study of XUV superfluorescence from doubly excited states of helium resonantly pumped by FEL pulses. Our model allows to predict both the spectrum and angular distribution of emitted XUV radiation in a wide range of experimentally accessible parameters. This is achieved by going beyond two key deficiencies of most previous models: the one-dimensional treatment in space is upgraded to three dimensions with electromagnetic fields treated in the paraxial approximation, and spontaneous emission is modeled by a recently developed approach that avoids the unrealistic delayed response but preserves the expected characteristics of the emitted field in the spontaneous emission limit. The case study of $3a\ ^1P^o$ resonance in helium with 63.66 eV excitation energy is presented for realistic parameters of seeded light pulses from the FERMI FEL facility and a newly developed high-pressure gas cell. Results of numerical simulations show that both the spectral width and angular divergence of emitted radiation vary with gas pressure and pump pulse intensity in a complex way.

I. INTRODUCTION

The development of free-electron lasers (FELs) [1–3] has opened the way for studying nonlinear interaction of extreme ultraviolet (XUV) and x-ray light with matter. One of such processes is superfluorescence [4], where spontaneously emitted radiation is amplified as it propagates through an inverted population of target atoms. Achieving a substantial population of excited states which rapidly decay via fluorescence in the XUV or x-ray spectral domain requires pumping by highly intense light pulses with duration on the order of femtoseconds, that are currently produced only by FELs. Superfluorescence has in recent years been observed in a range of different targets, for example in neon gas [5], copper foil [6] and manganese solutions [7]. In all of these experiments, strong amplification of fluorescence was observed along with an exponential dependence of the number of emitted photons on pump pulse energy.

Since the emitted light pulses have high longitudinal coherence and a duration that is comparable to that of FEL pulses [8, 9], there has been interest in employing superfluorescence as the basis for new implementations of x-ray lasers [10]. However, designing such elaborate instruments requires reliable theoretical predictions. Modeling of superfluorescence is an intricate problem, which has been extensively investigated in the optical domain [4], but has recently also received attention at shorter wavelengths [8, 9, 11]. Despite the progress in the theoretical description of XUV and x-ray superfluorescence, the agreement between predictions and experimental results is still only qualitative. One of the problems is an accurate description of spontaneous emission, which is the basis for subsequent amplification of the emitted field. This has most widely been modeled by adding stochastic noise terms mimicking fluctuations of polarization to the semiclassical Maxwell-Bloch equations [12, 13]. However, it has been shown [14] that the generally used form of the noise terms produces a delay in the emitted pulse with respect to pumping, and is thus inadequate for modeling systems in which pump pulse duration is comparable to the excited state lifetime.

Another reason for the poor agreement between theoretical and experimental results is that field propagation is generally modeled in a single spatial dimension. This is justified by the fact that typically in superfluorescence experiments the excited part of the target has the shape of an elongated cylinder. However, even in this case, the system evolution depends on the Fresnel number, which is proportional to the square of the target radius and inversely

proportional to the target length and emitted field wavelength, and is thus a measure of the significance of diffraction effects [4]. Strictly speaking, the one-dimensional spatial approximation is only adequate when the Fresnel number of the system is approximately one. The spatially one-dimensional approach also assumes that the intensity profile of pump radiation in the plane perpendicular to its propagation direction is uniform with a cut-off at a certain radius. Since the amplification of emitted radiation depends exponentially on the local intensity of the pump pulse, such a model cannot directly describe the propagation of pulses with a Gaussian lateral intensity profile, such as those produced by realistic FELs [1]. A Gaussian spatial intensity profile can be approximately accounted for by combining simulation results for the box-type intensity profile for different peak intensities [14]. However, such spatial averaging does not provide information on transverse variations of the emitted field intensity, and is only applicable if the Rayleigh range of the pump beam is much larger than the target length, so that diffraction of the FEL pulse inside the target is negligible. This is not the case in experiments with gas targets pumped by XUV pulses featuring focal sizes of a few micrometers and the Rayleigh range on the order of millimeters [15].

The typical experimental setup for observation of superfluorescence is the following: pump pulses are focused onto the target to create a long column of transiently excited atoms or ions. Amplified emission in the forward direction is analyzed with a dispersive spectrometer, diffracting the signal onto a 2D detector. The dispersive axis of the recorded images thus reflects the energy spectrum of superfluorescence pulses, whereas the nondispersive direction allows for observation of the spatial intensity profile of emitted radiation [5]. Recording the zero-order image on a CCD camera after filtering out the pump signal also allows to directly measure the transverse angular profile of superfluorescence with a resolution of approximately the ratio of pixel size and distance between the target and detector. However, due to the lack of 3D modeling, the latter aspect of the measurements has not yet been fully investigated. Modeling the spatial dependence of the emitted field intensity is also crucial for experiments in which the gain cannot be simply inferred from measurements of the emitted pulse energy. Such an example is the observation of seeded Mn $K\beta$ stimulated emission [16], where the target was irradiated with two-color FEL pulses. One color was used to create a core-hole population inversion, and the other to stimulate the weak $K\beta$ emission. Because of the lack of an upstream spectrometer that would measure the shot-by-shot seed pulse energy before the target, amplification of $K\beta$ emission was detected based on the angular

divergence of the amplified field with respect to the seed.

In this work we present a theoretical study of XUV superfluorescence from the $3a^1P^o$ doubly excited state of helium, resonantly pumped by FEL pulses with 63.66 eV photon energy (Fig. 1). The evolution of the system is described in three spatial dimensions and time, and the electromagnetic fields are propagated in the paraxial approximation. This is applicable since due to the elongated shape of the excited medium, emitted radiation primarily propagates along the cylinder axis even when taking into account its transverse variations. The duration of pump pulses is comparable to the 80 fs lifetime of the excited state, which predominantly decays via autoionization. To model spontaneous emission and the onset of amplification, the recently introduced form of stochastic noise terms [17] is added to the Maxwell-Bloch equations. We demonstrate that this approach reproduces the expected temporal and spectral profile of spontaneously emitted radiation in the paraxial approximation for the studied system.

The helium atom is the prototypical two-electron system, and as such it has been immensely studied over the years. In particular, the measurement of the double excitation spectrum [18] was one of the early ground-breaking applications of synchrotron radiation. The advent of XUV FEL sources has enabled the study of nonlinear effects in helium, such as resonant multi-photon excitation [19, 20] and superfluorescence at visible wavelengths [21]. While XUV amplified spontaneous emission from helium has not been observed before, superfluorescence from the $3a^1P^o$ doubly excited state was theoretically investigated in Ref. [22]. However, in this study, the system evolution was described in a single spatial dimension, and spontaneous emission was modeled using noise terms that introduced an artificial delay to the emitted field. This model could thus provide only qualitative predictions on the characteristics of superfluorescence. In the present work, we surpass the most prohibiting limitations of the previous model by treating the system evolution in three spatial dimensions with noise terms that adequately model spontaneous emission, as well as including resonant coupling in He^+ , which will be shown to significantly affect the spectral properties of emitted radiation after its amplification. The presented numerical results, which are calculated for realistically achievable pumping and target parameters, could thus be directly experimentally verified.

The paper is organized as follows: in Sec. II, the theoretical model of superfluorescence from doubly excited states of helium is described along with the methods used to numer-

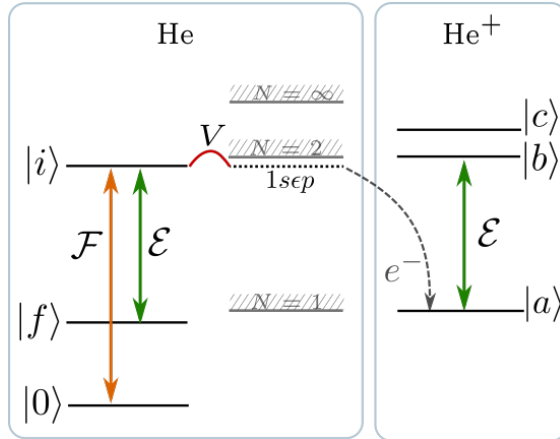


FIG. 1. Schematic representation of the level scheme. Helium atom in the ground state (0) is resonantly photoexcited to the selected doubly excited state (i), which is coupled to the continuum and decays via fluorescence to a singly excited state (f) or via autoionization to He⁺ $1s$ (a). The latter is coupled to He⁺ $2p$ (b) by the emitted radiation.

ically solve the obtained system of partial differential equations. Numerical results of the simulations and characteristics of superfluorescence in different regimes are discussed in Sec. III. Details of the derivation are presented in Appendix A, whereas the numerical values of photoionization cross sections used in the simulations are specified in Appendix B. In Appendix C, simulation results for the case of spontaneous emission are discussed, and the ability of stochastic noise terms to suitably describe spontaneous emission is verified. Atomic units are used throughout the paper, unless states otherwise.

II. THEORETICAL DESCRIPTION AND MODELING

The target is helium gas which is pumped by linearly polarized FEL pulses with 63.66 eV photon energy, resonant with the $1^1S^e \rightarrow 3a^1P^o$ transition ($|0\rangle \rightarrow |i\rangle$ in Fig. 1) [23]. This particular doubly excited state was selected for the present case study because it is relatively isolated in energy, so considering the pump spectral width, which is a few meV for seeded XUV FEL pulses [1], it is the only state that is excited. It has a lifetime of 80 fs [23] and decays predominantly by autoionization, resulting in a natural linewidth of 8.2 meV. The radiative decay contributes only $4.8 \mu\text{eV}$ [24] to the width, and the dominant radiative decay channel is to the singly excited 3^1S^e state ($|f\rangle$), with the emitted photon energy of

40.74 eV [25] and a fluorescence branching ratio of 72.7%. The final singly excited state has a lifetime of 55 ns [26]. Minor radiative decay channels of the doubly excited state are neglected, as it has been shown that emission from the dominant fluorescence channel is most strongly amplified and inclusion of minor channels does not significantly affect the evolution of superfluorescence [22].

Transition dynamics in the helium atom are modeled by a three-level Λ system, which is resonantly coupled to the $1s\epsilon p$ continuum (Fig. 1). This is a good approximation, since the linearly polarized pump field resonantly populates a single excited state, and this decays radiatively to a single final state by emission of radiation having the same linear polarization as the pump. The energy of photons emitted on the $|i\rangle - |f\rangle$ transition is relatively close to the 40.8 eV energy of $1s - 2p$ transition in He^+ with a $6.6 \mu\text{eV}$ natural width. The ground state of He^+ (denoted by $|a\rangle$) is strongly populated by autoionization of the doubly excited state, so in the saturation regime, where the spectral width of emitted radiation is expected to increase [9], significant field absorption due to the $\text{He}^+ 1s - 2p$ transition could occur, and the corresponding resonant coupling must be considered by the model. Spontaneous emission on this transition is neglected, since the $\text{He}^+ 2p$ excited state ($|b\rangle$) has a lifetime of 100 ps. Additionally, atomic and ionic states can be photoionized by the pump and emitted field. State $|c\rangle$ denotes a single level that is included to account for field absorption due to photoionization and effectively replaces excited states $\text{He}^+ nl$ with $n = 3, 4$. The latter is a reasonable approximation made to simplify the model, because resonant coupling of these states to each other or to the atomic states is negligible, and their populations are expected to be small.

A. Equations for atomic populations and coherences

Atomic states are coupled by the pump field F and emitted field E , with their main propagation direction parallel to the z axis. The transverse electric fields can be written in terms of their slowly varying amplitudes as

$$U = \mathcal{U}^{(+)} e^{i(k_{uz}z - \omega_U t)} + \mathcal{U}^{(-)} e^{-i(k_{uz}z - \omega_U t)}. \quad (1)$$

Here $U = F, E$ are the pump and emitted electric field, and $\mathcal{U}^{(\pm)} = \mathcal{F}^{(\pm)}, \mathcal{E}^{(\pm)}$ their respective positive- and negative-frequency components. Wave vector component along the

main propagation direction z and carrier frequency of the field U are denoted by k_{Uz} and ω_U , respectively. When modeling spontaneous emission with the addition of stochastic noise terms [17], the positive- and negative-frequency field amplitudes are not complex conjugate pairs. However, $|0\rangle - |i\rangle$ transition is resonantly pumped by a strong FEL pulse and branching ratio for the decay of the doubly excited state back to the ground state is about 50 times smaller than that for fluorescence into the final 3^1S^e state [27]. Stochastic noise contributions to the $|0\rangle - |i\rangle$ transition are thus negligible, and we can assume $\mathcal{F}^{(-)} = \mathcal{F}^{(+)*}$.

Following the derivation in Refs. [22, 28, 29], which is also outlined in Appendix A, we obtain a system of semiclassical Maxwell-Bloch equations that describe the evolution of the density matrix and propagation of electric field amplitudes in the paraxial and slowly varying envelope approximations [30]. In the retarded time frame, with $\tau = t - \alpha z$, the evolution of atomic populations is described by

$$\frac{\partial}{\partial \tau} \rho_{00} = -(\gamma_0 + \Gamma_0) \rho_{00} - i\mathcal{F}^{(-)} \tilde{\mu}_{0i} \left(1 - \frac{i}{q_{0i}}\right) \rho_{i0} + i\mathcal{F}^{(+)} \tilde{\mu}_{i0} \left(1 + \frac{i}{q_{i0}}\right) \rho_{0i}, \quad (2a)$$

$$\begin{aligned} \frac{\partial}{\partial \tau} \rho_{ii} = & -(\Gamma_a + \Gamma_r + \Gamma_i) \rho_{ii} - i\mathcal{F}^{(+)} \tilde{\mu}_{i0} \left(1 - \frac{i}{q_{i0}}\right) \rho_{0i} + i\mathcal{F}^{(-)} \tilde{\mu}_{0i} \left(1 + \frac{i}{q_{0i}}\right) \rho_{i0} \\ & - i\mathcal{E}^{(+)} \tilde{\mu}_{if} \left(1 - \frac{i}{q_{if}}\right) \rho_{fi} + i\mathcal{E}^{(-)} \tilde{\mu}_{fi} \left(1 + \frac{i}{q_{fi}}\right) \rho_{if} - \chi (h\rho_{fi} + h^\dagger \rho_{if}), \end{aligned} \quad (2b)$$

$$\begin{aligned} \frac{\partial}{\partial \tau} \rho_{ff} = & -(\gamma_f + \Gamma_f) \rho_{ff} + \Gamma_r^f \rho_{ii} - i\mathcal{E}^{(-)} \tilde{\mu}_{fi} \left(1 - \frac{i}{q_{fi}}\right) \rho_{if} + i\mathcal{E}^{(+)} \tilde{\mu}_{if} \left(1 + \frac{i}{q_{if}}\right) \rho_{fi} \\ & + \chi (h^\dagger \rho_{if} + h\rho_{fi}) + h^* \rho_{if} + h^\dagger \rho_{fi}. \end{aligned} \quad (2c)$$

Here $\Gamma_a = 8.2 \text{ meV}$ is the autoionization decay width of the doubly excited state, $\Gamma_r = 4.8 \mu\text{eV}$ its fluorescence width, $\Gamma_r^f = 3.5 \mu\text{eV}$ partial radiative rate to the final state, and $\gamma_{0,f}$ are field-induced widths of the ground and final state (see Appendix A). Nonresonant photoionization processes are encompassed in Γ_j , $j = 0, i, f$, that are added to the density matrix equations via a rate-equation approach and are defined as

$$\Gamma_0 = \Gamma_{\varepsilon 0}, \quad (3a)$$

$$\Gamma_i = \Gamma_{\mathcal{F}i} + \Gamma_{\varepsilon i}, \quad (3b)$$

$$\Gamma_f = \Gamma_{\mathcal{F}f}. \quad (3c)$$

Here Γ_{Uj} denotes the photoionization rate of state $|j\rangle$ with field U and can be expressed as $\Gamma_{Uj} = \sigma_{Uj} J_U$, where $J_U = \mathcal{U}^{(+)} \mathcal{U}^{(-)} / (2\pi\alpha\omega_U)$ is the flux of field U and σ_{Uj} the photoionization cross section specified in Appendix B. Ionization of the ground state with the emitted field

populates $\text{He}^+ 1s$, whereas ionization of the final state with the pump field and ionization of the doubly excited state with both fields populate the combined ionic state $|c\rangle$ (see Appendix B).

The modified dipole matrix elements $\tilde{\mu}_{ij} = \tilde{\mu}_{ji}$, $j = 0, f$, describe transitions to and from the discrete excited state modified by an admixture of the continuum [22], and q_{ij} are the real-valued Fano parameters [31]. For the present atomic system, the values of dipole moments are $\tilde{\mu}_{i0} = 0.0143$ a.u. and $\tilde{\mu}_{if} = 0.279$ a.u.. For the pumping transition $q_{i0} = -2.57$, so the resonant part of the absorption coefficient for the pump field exhibits an asymmetric Fano profile, whereas for the $|i\rangle - |f\rangle$ transition q_{if} was calculated to be 310, hence in the spontaneous emission limit the emitted field spectrum is modeled as a Lorentzian. Fano parameters q_{ij} and dipole matrix elements $\tilde{\mu}_{ij}$ were calculated using the method of complex rotation [32].

The terms proportional to $h^{(\dagger)}, h^{(\dagger)*}$ on the r.h.s of Eqs. (2b) and (2c) are stochastic noise terms mimicking spontaneous emission on the $|i\rangle - |f\rangle$ transition, with χ being a normalization factor [17, 33]. The derivation of stochastic terms for the studied case is presented in Appendix A, whereas in Appendix C we numerically demonstrate the validity of simulating spontaneous emission with this approach by comparing the numerical and analytical results in the limit of low target pressures and pump pulse intensities.

Coherences describing the pumping transition $|0\rangle - |i\rangle$ evolve according to

$$\begin{aligned} \frac{\partial}{\partial \tau} \rho_{i0} = & - \left(\frac{\Gamma_{i0}}{2} + \Gamma_{i0}^D - i\Delta_{\mathcal{F}} \right) \rho_{i0} - i\mathcal{F}^{(+)} \tilde{\mu}_{i0} \left(1 - \frac{i}{q_{i0}} \right) \rho_{00} + i\mathcal{F}^{(+)} \tilde{\mu}_{i0} \left(1 + \frac{i}{q_{i0}} \right) \rho_{ii} \\ & - i\mathcal{E}^{(+)} \tilde{\mu}_{if} \left(1 - \frac{i}{q_{if}} \right) \rho_{f0} - \chi h \rho_{f0}, \end{aligned} \quad (4a)$$

$$\begin{aligned} \frac{\partial}{\partial \tau} \rho_{0i} = & - \left(\frac{\Gamma_{i0}}{2} + \Gamma_{i0}^D + i\Delta_{\mathcal{F}} \right) \rho_{0i} - i\mathcal{F}^{(-)} \tilde{\mu}_{0i} \left(1 - \frac{i}{q_{0i}} \right) \rho_{ii} + i\mathcal{F}^{(-)} \tilde{\mu}_{0i} \left(1 + \frac{i}{q_{0i}} \right) \rho_{00} \\ & + i\mathcal{E}^{(-)} \tilde{\mu}_{fi} \left(1 + \frac{i}{q_{fi}} \right) \rho_{0f} - \chi h^\dagger \rho_{0f}, \end{aligned} \quad (4b)$$

where $\Gamma_{ij} = \Gamma_a + \Gamma_r + \Gamma_i + \Gamma_j + \gamma_j$ for $j = 0, f$, and $\Delta_{\mathcal{F}} = \omega_{\mathcal{F}} - (E_i - E_0)$ is the pump field frequency detuning (E_j are energies of atomic levels). The last two terms on the r.h.s of Eqs. (4) are proportional to ρ_{0f}, ρ_{f0} , and are significant only when the emitted field intensity is large. In the studied system, this only occurs after field amplification, when the contribution of spontaneous emission is already negligible and the emitted field amplitude can be described classically with $\mathcal{E}^{(-)} \approx \mathcal{E}^{(+)*}$. Consequently, stochastic noise terms in Eqs. (4) can be neglected, and we can assume $\rho_{i0} = \rho_{0i}^*$.

The Doppler line broadening is accounted for in an approximate way [34] by adding an extra decay rate $\Gamma_{ij}^D = \gamma_D |E_i - E_j|$ to the equations for nondiagonal density matrix elements, where $\gamma_D = [8 \ln(2) k_B T / (M c^2)]^{1/2} \approx 6.15 \times 10^{-6}$ at room temperature with M being the mass of helium atoms and T the gas temperature. Collisional processes are neglected, since for the gas pressures of interest both the elastic collisional rates between atoms [35] as well as electron-impact excitation and ionization rates [36] are much smaller than the autoionization or photoionization rates.

The time dependence of other nondiagonal matrix elements is described by

$$\begin{aligned} \frac{\partial}{\partial \tau} \rho_{if} = & - \left(\frac{\Gamma_{if}}{2} + \Gamma_{if}^D - i\Delta_\varepsilon \right) \rho_{if} - i\mathcal{E}^{(+)} \tilde{\mu}_{if} \left(1 - \frac{i}{q_{if}} \right) \rho_{ff} + i\mathcal{E}^{(+)} \tilde{\mu}_{if} \left(1 + \frac{i}{q_{if}} \right) \rho_{ii} \\ & - i\mathcal{F}^{(+)} \tilde{\mu}_{i0} \left(1 - \frac{i}{q_{i0}} \right) \rho_{0f} + \chi h (\rho_{ii} - \rho_{ff}) + h^{\dagger*} \rho_{ii}, \end{aligned} \quad (5a)$$

$$\begin{aligned} \frac{\partial}{\partial \tau} \rho_{fi} = & - \left(\frac{\Gamma_{if}}{2} + \Gamma_{if}^D + i\Delta_\varepsilon \right) \rho_{fi} - i\mathcal{E}^{(-)} \tilde{\mu}_{fi} \left(1 - \frac{i}{q_{fi}} \right) \rho_{ii} + i\mathcal{E}^{(-)} \tilde{\mu}_{fi} \left(1 + \frac{i}{q_{fi}} \right) \rho_{ff} \\ & + i\mathcal{F}^{(-)} \tilde{\mu}_{0i} \left(1 + \frac{i}{q_{0i}} \right) \rho_{f0} + \chi h^\dagger (\rho_{ii} - \rho_{ff}) + h^* \rho_{ii}, \end{aligned} \quad (5b)$$

$$\begin{aligned} \frac{\partial}{\partial \tau} \rho_{0f} = & - \left(\frac{\Gamma_{0f}}{2} + i[\Delta_{\mathcal{F}} - \Delta_\varepsilon] \right) \rho_{0f} - i\mathcal{F}^{(-)} \tilde{\mu}_{0i} \left(1 - \frac{i}{q_{0i}} \right) \rho_{if} + i\mathcal{E}^{(+)} \tilde{\mu}_{if} \left(1 + \frac{i}{q_{if}} \right) \rho_{0i} \\ & + (\chi h + h^{\dagger*}) \rho_{0i}, \end{aligned} \quad (5c)$$

$$\begin{aligned} \frac{\partial}{\partial \tau} \rho_{f0} = & - \left(\frac{\Gamma_{0f}}{2} - i[\Delta_{\mathcal{F}} - \Delta_\varepsilon] \right) \rho_{f0} - i\mathcal{E}^{(-)} \tilde{\mu}_{fi} \left(1 - \frac{i}{q_{fi}} \right) \rho_{i0} + i\mathcal{F}^{(+)} \tilde{\mu}_{i0} \left(1 + \frac{i}{q_{i0}} \right) \rho_{fi} \\ & + (\chi h^\dagger + h^*) \rho_{i0}, \end{aligned} \quad (5d)$$

with $\Delta_\varepsilon = \omega_\varepsilon - (E_i - E_f)$ being the emitted field detuning, and $\Gamma_{0f} = \sum_{j=0,f} (\Gamma_j + \gamma_j)$. Since in our case the only contribution to the emitted field stems from resonant fluorescence, $\Delta_\varepsilon = 0$.

B. Equations for ionic populations and coherences

Ionic states $|a\rangle$ and $|b\rangle$ effectively act as a two-level system, however, the equation governing the lower state population contains additional terms due to its resonant coupling to the doubly excited state:

$$\begin{aligned} \frac{\partial}{\partial \tau} \rho_{aa} = & - \Gamma_{\mathcal{F}a} \rho_{aa} + (\gamma_0 + \Gamma_{\varepsilon 0}) \rho_{00} + \Gamma_a \rho_{ii} + \gamma_f \rho_{ff} - i\mathcal{E}^{(-)} \mu_{ab} \rho_{ba} + i\mathcal{E}^{(+)} \mu_{ba} \rho_{ab} \\ & + 2 \frac{\tilde{\mu}_{i0}}{q_{i0}} \mathcal{F}^{(+)} \rho_{0i} + 2 \frac{\tilde{\mu}_{0i}}{q_{0i}} \mathcal{F}^{(-)} \rho_{i0} + 2 \frac{\tilde{\mu}_{if}}{q_{if}} \mathcal{E}^{(+)} \rho_{fi} + 2 \frac{\tilde{\mu}_{fi}}{q_{fi}} \mathcal{E}^{(-)} \rho_{if}, \end{aligned} \quad (6a)$$

$$\frac{\partial}{\partial \tau} \rho_{bb} = -(\Gamma_{\mathcal{F}b} + \Gamma_{\mathcal{E}b}) \rho_{bb} + i\mathcal{E}^{(-)} \mu_{ab} \rho_{ba} - i\mathcal{E}^{(+)} \mu_{ba} \rho_{ab}, \quad (6b)$$

$$\frac{\partial}{\partial \tau} \rho_{ab} = -\left(\frac{\Gamma_{ab}}{2} + i\Delta_{\mathcal{E}}^{\text{ion.}}\right) \rho_{ab} - i\mathcal{E}^{(-)} \mu_{ab} (\rho_{bb} - \rho_{aa}), \quad (6c)$$

$$\frac{\partial}{\partial \tau} \rho_{ba} = -\left(\frac{\Gamma_{ab}}{2} - i\Delta_{\mathcal{E}}^{\text{ion.}}\right) \rho_{ba} + i\mathcal{E}^{(+)} \mu_{ba} (\rho_{bb} - \rho_{aa}). \quad (6d)$$

Here $\mu_{ab} = \mu_{ba} = 0.372$ a.u., $\Gamma_{ab} = \Gamma_{\mathcal{F}a} + \Gamma_{\mathcal{F}b} + \Gamma_{\mathcal{E}b}$, and $\Delta_{\mathcal{E}}^{\text{ion.}} = \omega_{\mathcal{E}} - (E_b - E_a)$ with E_a and E_b being the energies of the He^+ $1s$ and $2p$ states, respectively. Other levels of He^+ are only coupled to the rest of the system through nonresonant photoionization, so the population of state $|c\rangle$, in which they are combined, evolves according to

$$\frac{\partial}{\partial \tau} \rho_{cc} = -(\Gamma_{\mathcal{F}c} + \Gamma_{\mathcal{E}c}) \rho_{cc} + (\Gamma_{\mathcal{F}i} + \Gamma_{\mathcal{E}i}) \rho_{ii} + \Gamma_{\mathcal{F}f} \rho_{ff}. \quad (7)$$

C. Field propagation equations

In the paraxial approximation, propagation of the slowly varying pump field amplitude is described by (see Appendix A) [4, 37]

$$\left(\frac{\partial}{\partial z} - \frac{i}{2k_{\mathcal{F}}} \nabla_{\perp}^2\right) \mathcal{F}^{(+)} = -\frac{\kappa_{\mathcal{F}}}{2} \mathcal{F}^{(+)} - 2\pi i \alpha \omega_{\mathcal{F}} n \tilde{\mu}_{0i} \left(1 - \frac{i}{q_{0i}}\right) \rho_{i0}, \quad (8)$$

where $\nabla_{\perp}^2 = (\partial^2/\partial x^2 + \partial^2/\partial y^2)$, n is the number density of atoms, and

$$\kappa_{\mathcal{F}} = n \left(\tilde{\sigma}_0 \rho_{00} + \sum_{j=i,f,a,b,c} \sigma_{\mathcal{F}j} \rho_{jj} \right) \quad (9)$$

is the pump field absorption coefficient. The FEL pump pulse impinging on the target is assumed to have an axially symmetric Gaussian transverse intensity profile with the focal point at longitudinal position z_0 (see Appendix A). The input parameters are the pulse energy E_{FEL} and spotsize d_0 in focus (FWHM of the intensity profile). The temporal profile of the pump pulse is also assumed to be Gaussian with a FWHM duration τ_0 , in accordance with temporally coherent pulses produced by the seeded FEL FERMI [1] that operates in the XUV spectral range.

Equations for the emitted field amplitudes are

$$\begin{aligned} \left(\frac{\partial}{\partial z} - \frac{i}{2k_{\mathcal{E}}} \nabla_{\perp}^2\right) \mathcal{E}^{(+)} = & -\frac{\kappa_{\mathcal{E}}}{2} \mathcal{E}^{(+)} - 2\pi i \alpha \omega_{\mathcal{E}} \left[n \tilde{\mu}_{fi} \left(1 - \frac{i}{q_{fi}}\right) \frac{\rho_{if} + \rho_{fi}^*}{2} + \tilde{\mu}_{fi} h \right. \\ & \left. + n \mu_{ab} \rho_{ba} \right], \end{aligned} \quad (10a)$$

$$\left(\frac{\partial}{\partial z} + \frac{i}{2k_\varepsilon} \nabla_\perp^2\right) \mathcal{E}^{(-)} = -\frac{\kappa_\varepsilon}{2} \mathcal{E}^{(-)} + 2\pi i \alpha \omega_\varepsilon \left[n \tilde{\mu}_{if} \left(1 + \frac{i}{q_{if}}\right) \frac{\rho_{fi} + \rho_{if}^*}{2} + \tilde{\mu}_{if} h^\dagger + n \mu_{ba} \rho_{ab} \right]. \quad (10b)$$

Due to the stochastic noise terms (terms proportional to h, h^\dagger) the positive- and negative-frequency amplitude components are not hermitian conjugates. The form of coherence terms (second term on r.h.s of each equation) arises from the regularization necessary because of divergent noise trajectories [17]. The absorption coefficient

$$\kappa_\varepsilon = n \left(\tilde{\sigma}_f \rho_{ff} + \sum_{j=0,i,b,c} \sigma_{\varepsilon_j} \rho_{jj} \right)$$

is the same for both amplitudes, as it only depends on the field flux and diagonal density matrix elements.

D. Numerical implementation

The system of differential equations is solved numerically on a discrete grid of points $(x_k, y_l, z_m, \tau_n) = (k\Delta x, l\Delta y, m\Delta z, n\Delta\tau)$. Differential equations for the density matrix are propagated as

$$\rho_{ij, x_k y_l z_m \tau_{n+1}} = \rho_{ij, x_k y_l z_m \tau_{n+1}} \Big|_{\text{reg.}} + \Delta\tau \rho_{ij, x_k y_l z_m \tau_n} \Big|_{\text{noise}}, \quad (11)$$

where $\rho_{ij, x_k y_l z_m \tau_{n+1}} \Big|_{\text{reg.}}$ is the regular part of the density matrix equations (without stochastic terms), which is propagated from time τ_n to τ_{n+1} using the 4th order Runge-Kutta method [38], and $\rho_{ij, x_k y_l z_m \tau_n} \Big|_{\text{noise}}$ is the stochastic part. On the discretized grid, the noise normalization factor is $\chi = \pi \alpha \omega_\varepsilon |\tilde{\mu}_{fi}|^2 \Delta z$ and the stochastic terms are defined as [17]

$$h_{x_k y_l z_m \tau_n} = \sqrt{\frac{1}{\chi \Delta V \Delta \tau}} \left[\sqrt{\frac{\rho_{ii}}{\rho_{ii} - \rho_{ff}}} \right]_{x_k y_l z_m \tau_n} \xi_{x_k y_l z_m \tau_n}, \quad (12a)$$

$$h_{x_k y_l z_m \tau_n}^\dagger = \sqrt{\frac{1}{\chi \Delta V \Delta \tau}} \left[\sqrt{\frac{\rho_{ii}}{\rho_{ii} - \rho_{ff}}} \right]_{x_k y_l z_m \tau_n} \xi_{x_k y_l z_m \tau_n}^\dagger, \quad (12b)$$

$$h_{x_k y_l z_m \tau_n}^* = \sqrt{\frac{\chi}{\Delta V \Delta \tau}} \left[\sqrt{\frac{\rho_{ii} - \rho_{ff}}{\rho_{ii}}} \right]_{x_k y_l z_m \tau_n} \xi_{x_k y_l z_m \tau_n}^*, \quad (12c)$$

$$h_{x_k y_l z_m \tau_n}^{\dagger*} = \sqrt{\frac{\chi}{\Delta V \Delta \tau}} \left[\sqrt{\frac{\rho_{ii} - \rho_{ff}}{\rho_{ii}}} \right]_{x_k y_l z_m \tau_n} \xi_{x_k y_l z_m \tau_n}^{\dagger*}, \quad (12d)$$

where $\Delta V = \Delta x \Delta y \Delta z$, and ξ, ξ^\dagger are complex random numbers drawn from a standard normal distribution at each grid point. Equations for the field propagation are solved by a split-step finite-difference beam propagation method [39, 40] (see Appendix A for details).

III. RESULTS AND DISCUSSION

Previous studies have shown [22] that the crucial parameter for achieving superfluorescence in gasses is a sufficiently high target density. This is usually achieved by using an open-end stationary or pulsed gas cell, or an Even-Lavie or Parker valve as the source [5, 41, 42], however, in these cases the spatial profile of gas density is generally unknown. Moreover, density along the pump pulse propagation direction rises and falls off slowly, causing unwanted absorption of the pump pulse where gas density is too small to achieve amplification. Another option is to use the recently developed microfluidic glass cells produced by femtosecond laser irradiation followed by chemical etching [43, 44], which allow to achieve a high gas density with a flat profile in a localized region. Such cells have been used for example to demonstrate the generation of few-cycle deep ultraviolet pulses via frequency upconversion [45], and to efficiently generate high-order harmonics in helium gas [46]. These devices appear ideal for superfluorescence experiments, since the gas density inside the cell can be finely tuned and pressures of up to 1 bar can be achieved [46]. As the aim of this study is to reproduce a realistic experimental setup as closely as possible, we will use a density profile that can be produced by a simple version of such a cell [45] and is shown on the left-hand side plot of Fig. 6. The (target or gas) pressure p specified throughout this section refers to the backing pressure in the reservoir that is connected to the cell by an injection channel. Gas density inside the cell scales linearly with backing pressure [46], and its maximum value is about 1% smaller than the density calculated from the ideal gas law using the value of the backing pressure. The length of the microfluidic cell is around 10 mm, and we assume that the focal point of the FEL beam is at the middle of the cell with a focal FWHM spot size of $d_0 = 6 \mu\text{m}$ and $\tau_0 = 50 \text{ fs}$ FWHM pulse duration, in line with parameters achievable at FERMI FEL [15]. Numerical results presented in this section are averaged over 300 repetitions of the simulation, unless stated otherwise.

In experiments with gas targets, it is possible to investigate the dependence of the superfluorescence yield from a given excited state on two parameters: target pressure and pump pulse energy. The number of emitted photons as function of these two parameters for the $3a \ ^1P^o$ resonance in He is shown in Fig. 2. Increasing either of the two parameters produces the same characteristic curve. At low pressures or pump pulse energies, the density of excited states is small and emission is spontaneous with a linear increase of the number of

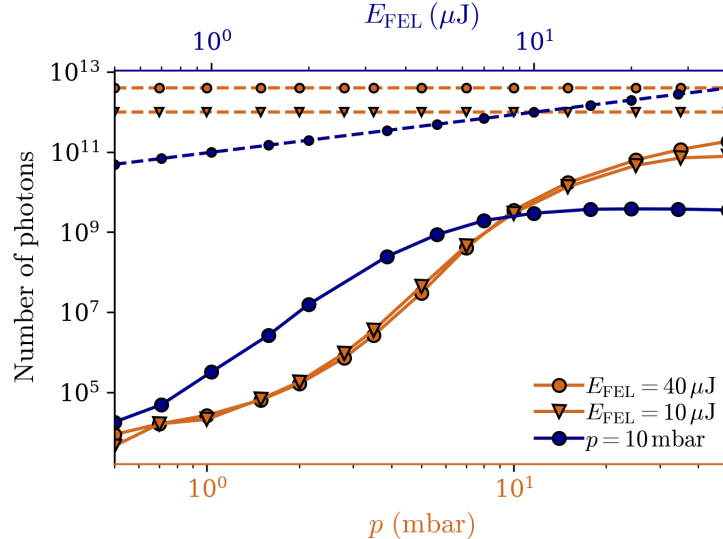


FIG. 2. Number of emitted photons as function of gas pressure and pump pulse energy. Dashed lines denote the corresponding number of pump photons impinging on the target.

emitted photons. When either of the two parameters is sufficiently high, the emitted field starts to amplify and the photon number increases exponentially, until the system reaches saturation at high gas pressures and/or pump pulse energies. In the latter regime, the dependence of the photon number on the two parameters can be anywhere from constant to linear, depending on the fraction of atoms that is excited from the ground state, or can even start to decrease at very high gas pressures, when emitted field absorption becomes the dominant process. At the highest investigated gas pressures, the number of emitted photons is only about an order of magnitude smaller than the number of photons in the FEL pulse impinging on the target.

A quantity that is generally measured in superfluorescence experiments is the spatially-integrated frequency spectrum of emitted radiation. In the spontaneous emission limit, the spectral profile is approximately Lorentzian with a width corresponding to the excited state lifetime (see Fig. 7(a)). The spectral shape remains roughly equal also in the amplification regime. While gain narrowing, i.e. a decrease in the bandwidth of emitted radiation, is expected to occur simultaneously with field amplification in high-gain systems [47], this is not observed here because the pump pulse duration is comparable to the excited state lifetime, and pumping modifies the excited state population as it decays. Increasing the pressure even further leads to a broadening of the spectral line, which also becomes highly

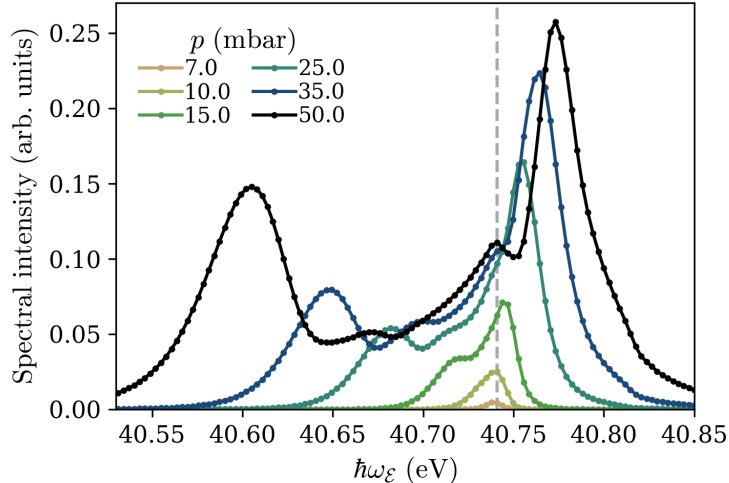


FIG. 3. Spectral intensity of radiation emitted from the target exit integrated over transverse dimensions for different backing pressures and $40 \mu\text{J}$ pump pulse energy. Dashed vertical line denotes the $|i\rangle - |f\rangle$ transition energy.

asymmetric. Figure 3 shows spatially-integrated frequency spectra of radiation emitted by the target for different backing pressures after the onset of saturation. Broadening of the spectral line is caused by the Autler-Townes effect and is characteristic of the saturation regime of superfluorescence [9, 22], however, its asymmetry is specific to the presented case. In part, the asymmetric profile is a consequence of the fact that radiation stems from an autoionizing resonance. This leads to a modified Autler-Townes effect producing a complex spectral shape [48], which can be observed in Fig. 3 for pressures below 20 mbar, when the emission line is still relatively narrow. Additionally, as the spectral line widens with increasing gas pressure, the high-energy part of the emission spectrum starts to overlap with the energy of $\text{He}^+ 1s - 2p$ transition at 40.8 eV. The emitted field is re-absorbed around this transition energy due to resonant excitation of He^+ ions in the ground state. Depending on the pressure and pump pulse energy, this absorption can be only partial; coupling of ionic states to the strong electric field produces Rabi oscillations in the time domain (see Fig. 6) and the corresponding broadening or splitting of the emission line in the spectral domain. In line with this, the spectral region of partial field re-absorption is not limited to a few μeV around 40.8 eV photon energy, as expected in the case of non-driven $\text{He}^+ 1s - 2p$ transition governed by the natural width.

In the XUV spectral region, directional radiation emitted from the target is usually ana-

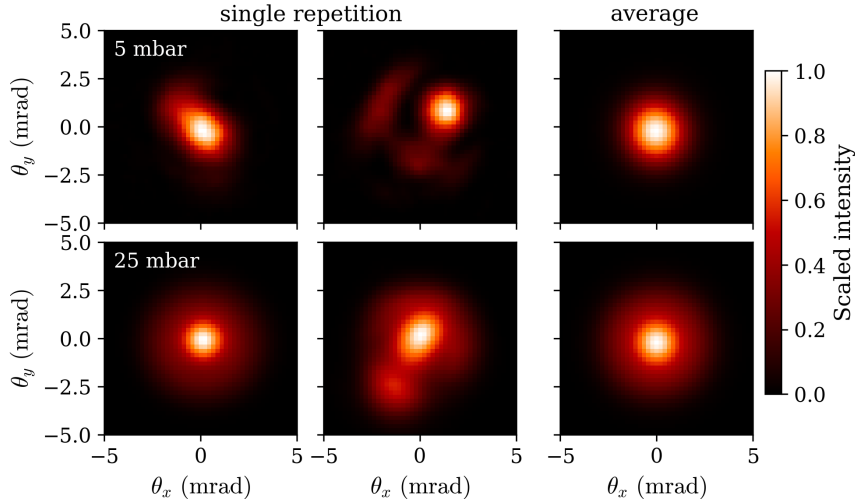


FIG. 4. Single-repetition and average time-integrated angular spectra of radiation emitted from the target exit for 5 mbar (first row) and 25 mbar backing pressure (second row), and $10 \mu\text{J}$ pump pulse energy.

lyzed using a grating spectrometer. In the Fraunhofer approximation, the zero-order image measured on a 2D detector typically positioned several meters from the target approximately corresponds to the time-integrated angular spectrum of emitted radiation. Examples of single-shot 2D angular spectra along with spectra averaged over 300 repetitions of the simulation for two different backing pressures are shown in Fig. 4. For the considered pump pulse energy of $10 \mu\text{J}$, the lower pressure of 5 mbar corresponds to the amplification regime of superfluorescence, whereas at the higher pressure of 25 mbar the system is in saturation. Single-shot angular spectra differ substantially between different repetitions of the simulation and can be highly asymmetric, with the peak of intensity positioned off-axis. This reflects the randomness of spontaneous emission which initiates the amplification process. On the other hand, average spectra exhibit cylindrical symmetry with maximum intensity at $\theta_{x,y} = 0$, as expected when pumping the target with a Gaussian beam. Average spectra differ for the two gas pressures, both in their shape as well as angular divergence.

More detailed changes of the angular spectral shape and divergence with varying gas pressure are demonstrated in Fig. 5. We define the angular divergence as the FWHM of average angular spectral intensity at either $\theta_x = 0$ or $\theta_y = 0$ mrad (average spectra are axially symmetric). At the lowest depicted pressures corresponding to initial stages of the amplification regime, the angular spectrum is approximately Gaussian, but angular

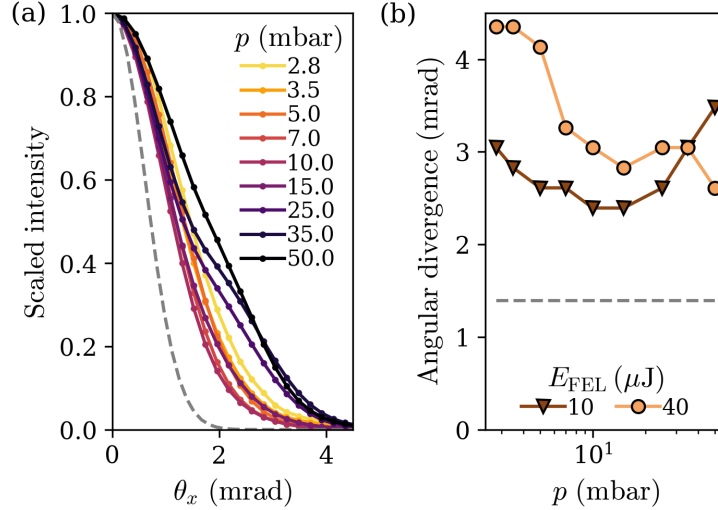


FIG. 5. (a) Scaled angular spectra of emitted radiation at $\theta_y = 0$ for different backing pressures and $10 \mu\text{J}$ pump pulse energy. (b) Angular divergence of the emitted field (see text) as function of backing pressure for two different pump pulse energies. Dashed gray lines denote the (a) angular spectrum and (b) angular divergence of the pump pulse.

divergence decreases with increasing pressure. This is a consequence of gain guiding; contrary to the case of spontaneous emission, which is approximately isotropic, in stimulated emission the field modes that are amplified are those propagating at small angles with respect to the pump propagation direction, because those are the modes that encounter a large population inversion and can thus be amplified. Moreover, the spatial profile of population inversion mimics that of the pump pulse, and thus has a Gaussian transverse profile. Since the rate of amplification is exponentially dependent on the local population inversion, its spatial distribution additionally contributes to the overall reduction of divergence.

As the gas pressure increases, parts of the gas close to the axis of pump pulse propagation enter saturation. However, field modes propagating off-axis might still undergo exponential amplification, since away from the target axis the overall field intensity is smaller and population inversion can remain positive. Consequently, in latter parts of the target, amplification of off-axis modes is relatively stronger than of those propagating at very small angles, hence the angular spectrum changes shape and divergence increases.

Depending on the combination of gas pressure and pump pulse energy, the transverse profile of population inversion can differ substantially from the Gaussian profile of the pump

pulse, and the maximum density of excited states can also vary longitudinally. The former occurs if the pump pulse is strong enough to completely deplete the ground state in some finite transverse region, whereas the latter takes place if the gas pressure is large and the pump pulse is significantly absorbed as it propagates through the target. Both cases can lead to a more complex dependence of the angular divergence, as shown for the $40 \mu\text{J}$ case in Fig. 5(b).

Overall, the angular divergence of the emitted pulse is significantly larger than that of the pump pulse. For all investigated gas pressures and both pump pulse intensities, angular divergence of the pump pulse after transition through the target is approximately 1.4 mrad . In terms of the angular spread of a Gaussian beam, which is defined in terms of its waist, this corresponds to 2.5 mrad , which is approximately in agreement with the expected angular spread of a Gaussian beam for the given focus size and wavelength (2.43 mrad) [49].

Analyzing the spatio-temporal dependence of emitted field intensity and population inversion shows that the dynamics of light-matter interaction are indeed highly nonuniform across the target, making 3D spatial modeling crucial for studies of superfluorescence. Figure 6 shows the (x, τ) dependence of these variables at $y = 0 \mu\text{m}$ and two different propagation distances z . The dependence of the emitted photon number on z is similar to the curves in Fig. 2, with a clearly discernible amplification and saturation region. Hence, the first longitudinal point $z = -2.8 \text{ mm}$ corresponds to the amplification regime, and the second point $z = 2.8 \text{ mm}$ to the saturation regime. Even though the quantities depicted in Fig. 6 cannot be directly measured, they can support the interpretation of results in Figs. 2 and 3, which can be experimentally verified.

At $z = -2.8 \text{ mm}$, population inversion in atomic helium $\rho_{ii} - \rho_{ff}$, which is created by resonant pumping with the FEL pulse, is positive and relatively large at short times. The main decay channel of the doubly excited state is autoionization to state $|a\rangle$, causing the population inversion in He^+ to be negative in the whole (x, t) region, since here the emitted field intensity is relatively small and resonant transfer of population to $\text{He}^+ 2p$ is negligible. The ground state of He^+ can be further photoionized to He^{2+} by the strong pump pulse, making the spatio-temporal dependence of population inversion more complex. The emitted field is delayed with respect to the pump pulse, as amplification requires some time to build up [9]. Since Fig. 6 shows results for a single repetition, the transverse dependence of the emitted field intensity is not symmetric with respect to $x = 0 \mu\text{m}$. However, this allows us

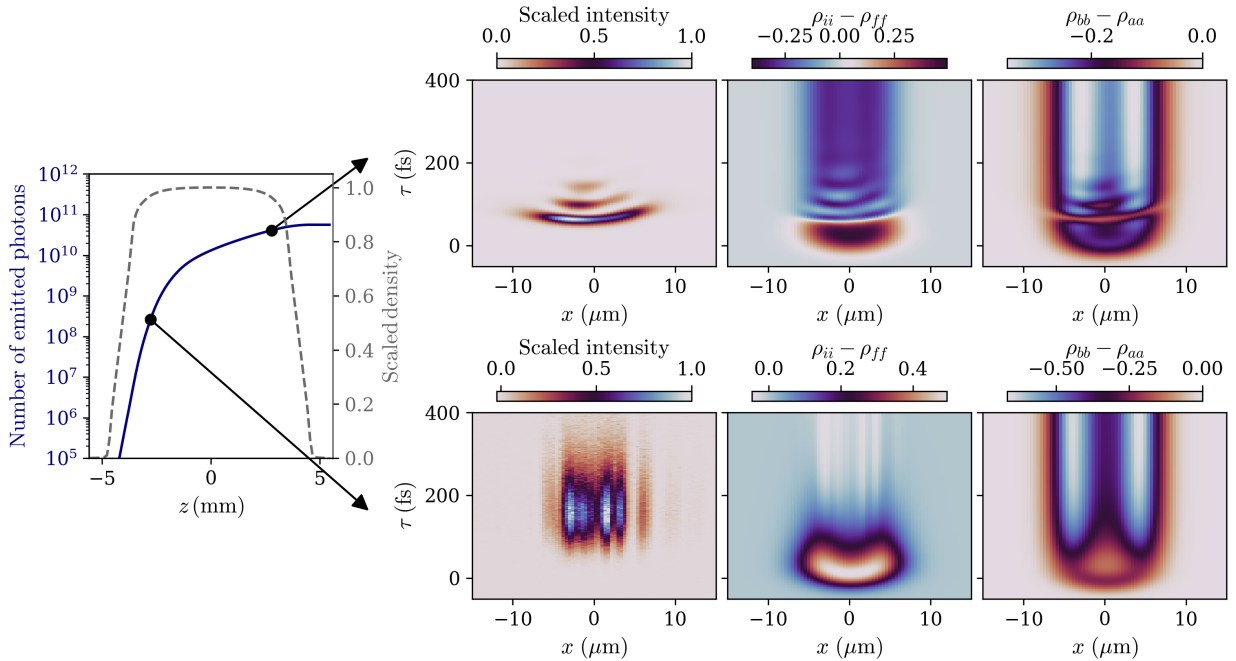


FIG. 6. Results of a single repetition of the simulation for 25 mbar backing pressure and $10 \mu\text{J}$ pump pulse energy. Left-hand side of the figure shows the number of emitted photons as function of propagation distance, along with the scaled longitudinal density profile of gas inside the microfluidic cell. Transverse (x, y) dependence of gas density is assumed to be constant. Plots on the right-hand side show the scaled emitted field intensity, population inversion in neutral helium $\rho_{ii} - \rho_{ff}$, and He^+ population inversion $\rho_{bb} - \rho_{aa}$ at $y = 0 \mu\text{m}$ for two propagation distances, i.e. $z = -2.8 \text{ mm}$ (bottom row) and $z = 2.8 \text{ mm}$ (top row), indicated by black dots on the left-hand side plot. Time $\tau = 0 \text{ fs}$ coincides with the peak of pump pulse intensity.

to observe that the regions of (x, τ) space where the emitted field intensity is significant coincide with the regions where $\rho_{ii} - \rho_{ff}$ becomes negative; these are the regions where due to stimulated emission population is transferred to the final state $|f\rangle$ by emission of an additional photon.

In the amplification regime at $z = 2.8 \text{ mm}$, Rabi oscillations are clearly visible both in the emitted field intensity and $\rho_{ii} - \rho_{ff}$ population inversion, where again the high-intensity regions coincide with a larger population of the final state. In the spectral domain, these oscillations correspond to a broadening of the emission line, as seen in Fig. 3. At long times, He population inversion around the target axis is more negative than in the amplification regime, which indicates that transfer of population to state $|f\rangle$ is stronger resulting in a

larger number of emitted photons. A clear manifestation of Rabi oscillations also in the He^+ population inversion confirms that the emitted field is indeed partially reabsorbed around the resonant energy of the $|a\rangle - |b\rangle$ transition. The spectral line there is broadened beyond the natural width due to coupling with strong electric fields, leading to the non-trivial calculated spectral shapes at high gas pressures (Fig. 3).

IV. CONCLUSIONS

We presented the results of a theoretical model of XUV superfluorescence emitted by helium atoms in a doubly excited state that is resonantly pumped by FEL light pulses. The model provides quantitative predictions that could be directly verified in an experimental campaign. The evolution of light-matter interaction is described in three spatial dimensions and time, and electric fields are treated in the paraxial approximation, which is a realistic 3D approximation due to the elongated shape of the active medium. Spontaneous emission, which initiates superfluorescence and thus crucially determines its evolution, is modeled by a recently developed form of stochastic noise terms that reproduce the expected properties of emitted radiation at low density of atoms in the resonant state.

The developed model enables the study of both the frequency and angular distribution of the emitted electric field, which are observables that could be measured with spectroscopic setups adapted to superfluorescence experiments. Characteristics of the emitted field are investigated for a wide range of experimentally achievable gas pressures and pump pulse energies. Simulation results show that the spectral width of emitted radiation increases significantly with increasing excited state density, and the distribution of spectral intensity exhibits a complex profile resulting from several processes. The angular divergence of the emitted field also varies with increasing gas pressure or pump pulse energy, and is calculated to be significantly larger than that of the pump beam. The latter is in line with experimental observation of seeded Mn $K\beta$ emission [16], where field amplification was detected based on the large angular divergence of emitted radiation.

While the model takes into account a wide array of atomic processes, some approximations are still made in the derivation of Maxwell-Bloch equations that limit the usability of the presented theoretical description. One of them is neglecting the minor radiative decay channels of the doubly excited state that could potentially get amplified after emission

on the dominant radiative transition becomes saturated [9], although it has been shown in the frame of a spatially one-dimensional model that this should not significantly alter the simulation results [22]. Another limiting approximation is neglecting the shifts associated with autoionization and field-induced ionization (see Appendix A). These could become significant at very large pump pulse energies or target pressures, and hence limit the range of parameters that can be studied with the presented model. Finally, at large gas pressures, plasma effects and electronic collisional processes could alter the dynamics of the system evolution, or the propagation length at which the system reaches saturation could become comparable to the transverse extent of the target, which would make the paraxial approximation no longer applicable. Experimental investigation of resonantly pumped XUV superfluorescence, which has not been observed before and is feasible for the studied atomic system, is thus crucial for the evaluation of the presented theoretical results.

V. ACKNOWLEDGEMENTS

This work is supported by the research programme No. P1-0112, and by the research project No. J1-3012 of the Slovenian Research Agency. The authors gratefully acknowledge the SLING consortium for funding this research by providing computing resources of the HPC system NSC at Jožef Stefan Institute. We are indebted to R. M. Vazquez from Istituto di Fotonica e Nanotecnologie in Milan (IFN-CNR) for the calculation of the helium density profile in the microfluidic gas cell, and to A. Halavanau from SLAC National Accelerator Laboratory for the discussions on stochastic noise terms.

-
- [1] E. Allaria *et al.*, [Nature Photonics](#) **6**, 699 (2012).
 - [2] P. Emma *et al.*, [Nature Photonics](#) **4**, 641 (2010).
 - [3] D. Pile, [Nature Photonics](#) **5**, 456 (2011).
 - [4] M. Gross and S. Haroche, [Physics Reports](#) **93**, 301 (1982).
 - [5] N. Rohringer, D. Ryan, R. A. London, M. Purvis, F. Albert, J. Dunn, J. D. Bozek, C. Bostedt, A. Graf, R. Hill, S. P. Hau-Riege, and J. J. Rocca, [Nature](#) **481**, 488 (2012).
 - [6] H. Yoneda, Y. Inubushi, K. Nagamine, Y. Michine, H. Ohashi, H. Yumoto, K. Yamauchi, H. Mimura, H. Kitamura, T. Katayama, T. Ishikawa, and M. Yabashi, [Nature](#) **524**, 446

- (2015).
- [7] T. Kroll, C. Weninger, R. Alonso-Mori, D. Sokaras, D. Zhu, L. Mercadier, V. P. Majety, A. Marinelli, A. Lutman, M. W. Guetg, F.-J. Decker, S. Boutet, A. Aquila, J. Koglin, J. Koralek, D. P. DePonte, J. Kern, F. D. Fuller, E. Pastor, T. Fransson, Y. Zhang, J. Yano, V. K. Yachandra, N. Rohringer, and U. Bergmann, *Phys. Rev. Lett.* **120**, 133203 (2018).
 - [8] C. Weninger and N. Rohringer, *Phys. Rev. A* **90**, 063828 (2014).
 - [9] Š. Krušič, K. Bučar, A. Mihelič, and M. Žitnik, *Phys. Rev. A* **102**, 013102 (2020).
 - [10] A. Halavanau, A. Benediktovitch, A. A. Lutman, D. DePonte, D. Cocco, N. Rohringer, U. Bergmann, and C. Pellegrini, *Proceedings of the National Academy of Sciences* **117**, 15511 (2020).
 - [11] A. Benediktovitch, V. P. Majety, and N. Rohringer, *Phys. Rev. A* **99**, 013839 (2019).
 - [12] P. D. Drummond and M. G. Raymer, *Phys. Rev. A* **44**, 2072 (1991).
 - [13] O. Larroche, D. Ros, A. Klisnick, A. Sureau, C. Möller, and H. Guennou, *Phys. Rev. A* **62**, 043815 (2000).
 - [14] Š. Krušič, K. Bučar, A. Mihelič, and M. Žitnik, *Phys. Rev. A* **98**, 013416 (2018).
 - [15] M. Zangrando, D. Cocco, C. Fava, S. Gerusina, R. Gobessi, N. Mahne, E. Mazzucco, L. Raimondi, L. Rumiz, and C. Svetina, *Journal of Synchrotron Radiation* **22**, 565 (2015).
 - [16] T. Kroll, C. Weninger, F. D. Fuller, M. W. Guetg, A. Benediktovitch, Y. Zhang, A. Marinelli, R. Alonso-Mori, A. Aquila, M. Liang, J. E. Koglin, J. Koralek, D. Sokaras, D. Zhu, J. Kern, J. Yano, V. K. Yachandra, N. Rohringer, A. Lutman, and U. Bergmann, *Phys. Rev. Lett.* **125**, 037404 (2020).
 - [17] A. Benediktovitch *et al.*, “Stochastic modeling of paraxial x-ray superfluorescence,” (2022), in preparation.
 - [18] R. P. Madden and K. Codling, *Phys. Rev. Lett.* **10**, 516 (1963).
 - [19] M. Nagasono, E. Suljoti, A. Pietzsch, F. Hennies, M. Wellhöfer, J.-T. Hoefft, M. Martins, W. Wurth, R. Treusch, J. Feldhaus, J. R. Schneider, and A. Föhlisch, *Phys. Rev. A* **75**, 051406 (2007).
 - [20] A. Hishikawa, M. Fushitani, Y. Hikosaka, A. Matsuda, C.-N. Liu, T. Morishita, E. Shigemasa, M. Nagasono, K. Tono, T. Togashi, H. Ohashi, H. Kimura, Y. Senba, M. Yabashi, and T. Ishikawa, *Phys. Rev. Lett.* **107**, 243003 (2011).
 - [21] K. Nakajima *et al.*, *Journal of the Physical Society of Japan* **84**, 054301 (2015).

- [22] Š. Krušič, K. Bučar, A. Mihelič, and M. Žitnik, *Phys. Rev. A* **99**, 013429 (2019).
- [23] J. M. Rost, K. Schulz, M. Domke, and G. Kaindl, *Journal of Physics B: Atomic, Molecular and Optical Physics* **30**, 4663 (1997).
- [24] C.-N. Liu, M.-K. Chen, and C. D. Lin, *Phys. Rev. A* **64**, 010501 (2001).
- [25] A. Burgers, D. Wintgen, and J. M. Rest, *Journal of Physics B: Atomic, Molecular and Optical Physics* **28**, 3163 (1995).
- [26] C. E. Theodosiou, *Atomic Data and Nuclear Data Tables* **36**, 97 (1987).
- [27] J. Söderström, M. Agåker, A. Zimina, R. Feifel, S. Eisebitt, R. Follath, G. Reichardt, O. Schwarzkopf, W. Eberhardt, A. Mihelič, M. Žitnik, and J.-E. Rubensson, *Phys. Rev. A* **77**, 012513 (2008).
- [28] A. Mihelič, M. Žitnik, and M. Hrast, *Journal of Physics B: Atomic, Molecular and Optical Physics* **50**, 245602 (2017).
- [29] A. Mihelič and M. Žitnik, *Phys. Rev. A* **91**, 063409 (2015).
- [30] L. Lugiato, F. Prati, and M. Brambilla, *Nonlinear optical systems* (Cambridge University Press, 2015).
- [31] U. Fano, *Phys. Rev.* **124**, 1866 (1961).
- [32] Y. Ho, *Physics Reports* **99**, 1 (1983).
- [33] S. Chuchurka *et al.*, “Stochastic methodology for superfluorescence i: General theory,” (2022), in preparation.
- [34] C. Ohae, J. R. Harries, H. Iwayama, K. Kawaguchi, S. Kuma, Y. Miyamoto, M. Nagasono, K. Nakajima, I. Nakano, E. Shigemasa, N. Sasao, S. Uetake, T. Wakabayashi, A. Yoshimi, K. Yoshimura, and M. Yoshimura, *Journal of the Physical Society of Japan* **85**, 034301 (2016).
- [35] R. Loudon, *The Quantum Theory of Light* (OUP Oxford, 2000) Chap. 2.9.
- [36] Y. Ralchenko, R. Janev, T. Kato, D. Fursa, I. Bray, and F. de Heer, *Atomic Data and Nuclear Data Tables* **94**, 603 (2008).
- [37] P. Lambropoulos and D. Petrosyan, *Fundamentals of quantum optics and quantum information*, Vol. 23 (Springer, 2007).
- [38] K. E. Atkinson, *An Introduction to Numerical Analysis* (Wiley, 1989).
- [39] S. A. Chin and C. R. Chen, *The Journal of Chemical Physics* **117**, 1409 (2002).
- [40] D. P. Kelly, *J. Opt. Soc. Am. A* **31**, 755 (2014).

- [41] J. R. Harries, H. Iwayama, S. Kuma, M. Iizawa, N. Suzuki, Y. Azuma, I. Inoue, S. Owada, T. Togashi, K. Tono, M. Yabashi, and E. Shigemasa, [Phys. Rev. Lett. **121**, 263201 \(2018\)](#).
- [42] L. Mercadier, A. Benediktovitch, C. Weninger, M. A. Blessohl, S. Bernitt, H. Bekker, S. Dobrodey, A. Sanchez-Gonzalez, B. Erk, C. Bomme, R. Boll, Z. Yin, V. P. Majety, R. Steinbrügge, M. A. Khalal, F. Penent, J. Palaudoux, P. Lablanquie, A. Rudenko, D. Rolles, J. R. Crespo López-Urrutia, and N. Rohringer, [Phys. Rev. Lett. **123**, 023201 \(2019\)](#).
- [43] R. Osellame, H. Hoekstra, G. Cerullo, and M. Pollnau, [Laser & Photonics Reviews **5**, 442 \(2011\)](#).
- [44] K. C. Vishnubhatla, N. Bellini, R. Ramponi, G. Cerullo, and R. Osellame, [Opt. Express **17**, 8685 \(2009\)](#).
- [45] M. Galli, V. Wanie, D. P. Lopes, E. P. Månsson, A. Trabattoni, L. Colaizzi, K. Saraswathula, A. Cartella, F. Frassetto, L. Poletto, F. Légaré, S. Stagira, M. Nisoli, R. M. Vázquez, R. Osellame, and F. Calegari, [Opt. Lett. **44**, 1308 \(2019\)](#).
- [46] A. G. Ciriolo, R. M. Vázquez, V. Tosa, A. Frezzotti, G. Crippa, M. Devetta, D. Faccialá, F. Frassetto, L. Poletto, A. Pusala, C. Vozzi, R. Osellame, and S. Stagira, [Journal of Physics: Photonics **2**, 024005 \(2020\)](#).
- [47] J. C. MacGillivray and M. S. Feld, [Phys. Rev. A **14**, 1169 \(1976\)](#).
- [48] S. I. Themelis, P. Lambropoulos, and M. Meyer, [Journal of Physics B: Atomic, Molecular and Optical Physics **37**, 4281 \(2004\)](#).
- [49] W. H. Carter, [Applied Optics **19**, 1027 \(1980\)](#).
- [50] P. Lambropoulos and P. Zoller, [Phys. Rev. A **24**, 379 \(1981\)](#).
- [51] G. Alber and P. Zoller, [Phys. Rev. A **27**, 1373 \(1983\)](#).
- [52] E. Paspalakis, N. J. Kylstra, and P. L. Knight, [Phys. Rev. A **60**, 642 \(1999\)](#).
- [53] P. Knight, M. Lauder, and B. Dalton, [Physics Reports **190**, 1 \(1990\)](#).
- [54] J. M. Carcione, F. Cavallini, J. Ba, W. Cheng, and A. N. Qadrouh, [Rheologica Acta **58**, 21 \(2019\)](#).
- [55] L. B. Madsen, P. Schlagheck, and P. Lambropoulos, [Phys. Rev. A **62**, 062719 \(2000\)](#).
- [56] S. Chuchurka *et al.*, “Quantum stochastic trajectories for particles and fields based on positive p representation,” (2022), in preparation.
- [57] S. Chuchurka *et al.*, “Stochastic methodology for superfluorescence ii: Mean field theory,” (2022), in preparation.

- [58] D. Arsenović, J. Dimitrijević, and B. Jelenković, *Communications in Nonlinear Science and Numerical Simulation* **67**, 264 (2019).
- [59] A. Mihelič, *Phys. Rev. A* **98**, 023409 (2018).
- [60] A. Mihelič and M. Horvat, *Phys. Rev. A* **103**, 043108 (2021).
- [61] M. Žitnik, A. Stanič, K. Bučar, J. G. Lambourne, F. Penent, R. I. Hall, and P. Lablanquie, *Journal of Physics B: Atomic, Molecular and Optical Physics* **36**, 4175 (2003).

Appendix A: Derivation of Maxwell-Bloch equations

The effective Hamiltonian which describes the atomic system interacting with resonant electromagnetic fields (Fig. 1) in the rotating wave approximation is [50–52]

$$\begin{aligned}
H = & \sum_{j=0,i,f} E_j |j\rangle\langle j| + \sum_{j=a,b} \int (E_j + \epsilon) |j\epsilon\rangle\langle j\epsilon| d\epsilon + \mathcal{F}^{(+)} \mu_{i0} \theta_{\mathcal{F}} |i\rangle\langle 0| + \mathcal{F}^{(-)} \mu_{0i} \theta_{\mathcal{F}}^* |0\rangle\langle i| + \\
& \mathcal{E}^{(+)} \mu_{if} \theta_{\mathcal{E}} |i\rangle\langle f| + \mathcal{E}^{(-)} \mu_{fi} \theta_{\mathcal{E}}^* |f\rangle\langle i| + \int d\epsilon \left(\mathcal{F}^{(+)} \mu_{a0} \theta_{\mathcal{F}} |a\epsilon\rangle\langle 0| + \mathcal{F}^{(-)} \mu_{0a} \theta_{\mathcal{F}}^* |0\rangle\langle a\epsilon| + \right. \\
& \mathcal{E}^{(+)} \mu_{af} \theta_{\mathcal{E}} |a\epsilon\rangle\langle f| + \mathcal{E}^{(-)} \mu_{fa} \theta_{\mathcal{E}}^* |f\rangle\langle a\epsilon| + V_{ia} |i\rangle\langle a\epsilon| + V_{ai} |a\epsilon\rangle\langle i| + \mathcal{E}^{(+)} \mu_{ba} \theta_{\mathcal{E}} |b\epsilon\rangle\langle a\epsilon| + \\
& \left. \mathcal{E}^{(-)} \mu_{ab} \theta_{\mathcal{E}}^* |a\epsilon\rangle\langle b\epsilon| \right)
\end{aligned} \quad (\text{A1})$$

where E_j is the unperturbed energy of state j , $E_a + \epsilon$ ($E_b + \epsilon$) energy of the $1s\epsilon p$ ($2p\epsilon p$) continuum state, $\mu_{jk} = \langle j|\hat{\mu}|k\rangle$ are the dipole matrix elements with $\hat{\mu}$ being the projection of electric dipole moment onto the field polarization vector, and for shorter notation we introduced $\theta_{\mathcal{U}} = \exp(ik_{\mathcal{U}z}z - i\omega_{\mathcal{U}}t)$, $\mathcal{U} = \mathcal{F}, \mathcal{E}$. Continuum states above the $N = 1$ ionization threshold are coupled to the doubly excited state via interaction \hat{V} , with $V_{jk} = \langle j|\hat{V}|k\rangle$. Ionic state $|c\rangle$ is only populated through nonresonant processes, so it is omitted from the Hamiltonian and will be coupled to the atomic system at a later stage via the corresponding photoionization rates [30].

By writing the solutions of the time-dependent Schrodinger equation in terms of the slowly varying probability amplitudes of resonantly coupled states u_j as

$$|\psi\rangle = e^{-iE_0 t} \left(u_0 |0\rangle + u_i \theta_{\mathcal{F}} |i\rangle + u_f \theta_{\mathcal{F}} \theta_{\mathcal{E}}^* |f\rangle + \int d\epsilon (u_{a\epsilon} \theta_{\mathcal{F}} |a\epsilon\rangle + u_{b\epsilon} \theta_{\mathcal{F}} \theta_{\mathcal{E}} |b\epsilon\rangle) \right), \quad (\text{A2})$$

we arrive at the following equations for the time evolution of probability amplitudes:

$$\frac{\partial}{\partial t} u_0 = -i\mathcal{F}^{(-)} \mu_{0i} u_i - i \int d\epsilon \mathcal{F}^{(-)} \mu_{0a} u_{a\epsilon}, \quad (\text{A3a})$$

$$\frac{\partial}{\partial t} u_i = i\Delta_{\mathcal{F}} u_i - i\mathcal{F}^{(+)} \mu_{i0} u_0 - i\mathcal{E}^{(+)} \mu_{if} u_f - i \int d\epsilon V_{ia} u_{a\epsilon}, \quad (\text{A3b})$$

$$\frac{\partial}{\partial t} u_f = i(E_0 + \omega_{\mathcal{F}} - E_f - \omega_{\mathcal{E}}) u_f - i\mathcal{E}^{(-)} \mu_{fi} u_i - i \int d\epsilon \mathcal{E}^{(-)} \mu_{fa} u_{a\epsilon}, \quad (\text{A3c})$$

$$\frac{\partial}{\partial t} u_{a\epsilon} = i\Delta_a(\epsilon) u_{a\epsilon} - i\mathcal{F}^{(+)} \mu_{a0} u_0 - iV_{ai} u_i - i\mathcal{E}^{(+)} \mu_{af} u_f - i\mathcal{E}^{(-)} \mu_{ab} u_{b\epsilon}, \quad (\text{A3d})$$

$$\frac{\partial}{\partial t} u_{b\epsilon} = i\Delta_b(\epsilon) u_{b\epsilon} - i\mathcal{E}^{(+)} \mu_{ba} u_{a\epsilon} \quad (\text{A3e})$$

and analogous equations for complex conjugate amplitudes, with $\Delta_a(\epsilon) = E_0 + \omega_{\mathcal{F}} - (E_a + \epsilon)$ and $\Delta_b(\epsilon) = E_0 + \omega_{\mathcal{F}} + \omega_{\mathcal{E}} - (E_b + \epsilon)$. By using the Born-Markov approximation [53] for the terms coupling continuum and atomic states, equations for amplitudes $u_{a\epsilon}, u_{a\epsilon}^*$ at time t can be formally solved to obtain (spatial coordinates are omitted)

$$u_{a\epsilon}(t) = \frac{\mathcal{F}^{(+)}(t) \mu_{a0} u_0(t) + \mathcal{E}^{(+)}(t) \mu_{af} u_f(t) + V_{ai} u_i(t)}{\Delta_a(\epsilon) + i\eta} - i \int_0^t dt' e^{-i\Delta_a(\epsilon)(t-t')} \mathcal{E}^{(-)}(t') \mu_{ab} u_{b\epsilon}(t') \quad (\text{A4a})$$

$$u_{a\epsilon}^*(t) = \frac{\mathcal{F}^{(-)}(t) \mu_{0a} u_0^*(t) + \mathcal{E}^{(-)}(t) \mu_{fa} u_f^*(t) + V_{ia} u_i^*(t)}{\Delta_a(\epsilon) - i\eta} + i \int_0^t dt' e^{i\Delta_a(\epsilon)(t-t')} \mathcal{E}^{(+)}(t') \mu_{ba} u_{b\epsilon}^*(t'), \quad (\text{A4b})$$

where we assume the limit $\eta \rightarrow 0^+$.

After inserting these solutions into Eqs. (A3) and analogous equations for the complex conjugate amplitudes, and neglecting the coupling of atomic states through the $2p\epsilon p$ continuum (terms proportional to $V_{ia}\mu_{ab}$ and $\mu_{ja}\mu_{ab}$, $j = 0, f$), we can make use of the Sokhotski-Plemelj theorem [54] to define the autoionization width $\Gamma_a = 2\pi|V_{ia}|_{\Delta_a(\epsilon)=0}^2$ and the associated shift [50], as well as the field-induced ionization widths $\gamma_0 = \tilde{\sigma}_0 J_{\mathcal{F}}$, $\gamma_f = \tilde{\sigma}_f J_{\mathcal{E}}$ and their associated shifts [55]. Ionization cross sections of the ground state with the pump field and final state with the emitted field are defined as $\tilde{\sigma}_j = 4\pi^2 \alpha \omega_{\mathcal{U}} |\mu_{ja}|_{\Delta_a(\epsilon)=0}^2$ with $j = 0, f$ and $\mathcal{U} = \mathcal{F}, \mathcal{E}$, respectively. In a similar way we can define the modified dipole matrix elements

$$\tilde{\mu}_{ij} = \mu_{ij} + \mathcal{P} \int d\epsilon \frac{V_{ia} \mu_{aj}}{\Delta_a(\epsilon)}, \quad j = 0, f, \quad (\text{A5})$$

that describe coupling of the ground or final state to the doubly excited state modified by the admixture of the continuum (\mathcal{P} denotes the Cauchy principal value). The Fano asymmetry parameters are then defined as $q_{ij} = \tilde{\mu}_{ij} / (\pi V_{ia} \mu_{aj})_{\Delta_a(\epsilon)=0}$ [31].

Density matrix equations for the atomic part of the system are obtained after neglecting the autoionization and field-induced shifts [48], as well as coupling of the ground and final

state through the 1sep continuum (terms proportional to $\mu_{ja}\mu_{ak}$, where $j = 0, f$ and $k = f, 0$, respectively) [22], and using $\rho_{jk} = u_j u_k^*$ as the definition of density matrix elements. Adding the rates due to nonresonant photoionization and fluorescence from the excited to final state leads to Eqs. (2-5). Ionic density matrix elements are defined as $\rho_{jk} = \int u_{j\epsilon} u_{k\epsilon}^* d\epsilon$ with $j, k = a, b$, from which Eqs. (6) are obtained after performing the same approximations as above.

The noise contribution to equations for the time evolution of density matrix elements is (see Refs. [17, 33, 56, 57])

$$\begin{aligned} \frac{\partial}{\partial t} \rho_{ij} \Big|_{\text{noise}} = & - \sum_{\sigma, s} \chi \left[\rho_{sj} T_{is\sigma} (H_{is} h - H_{si} h^\dagger) - \rho_{is} T_{sj\sigma} (H_{sj} h - H_{js} h^\dagger) \right] \\ & + \sum_{\sigma, s} \left[\rho_{sj} T_{is\sigma} H_{si} h^* + \rho_{is} T_{sj\sigma} H_{sj} h^{\dagger*} \right], \end{aligned} \quad (\text{A6})$$

where $H_{ij} = \Theta(E_i - E_j)$ with $\Theta(x)$ being the Heaviside step function. Tensor $T_{jk\sigma}$ describes the relative strength of dipole transitions between atomic states. Index σ runs over the field polarization modes, and s over the states of the system. In our case, since the pump field is linearly polarized, a single excited state is populated, and this decays radiatively to a single final state, so the emitted field contains only one polarization mode and index σ can be omitted. As mentioned in the main text, spontaneous decay to the ground state is neglected, thus

$$T_{jk} = \begin{bmatrix} 0 & 0 & 0 \\ 0 & 0 & 1 \\ 0 & 1 & 0 \end{bmatrix}, \quad (\text{A7})$$

where the sequence of states is $(0, i, f)$. Inserting Eq. (A7) into Eq. (A6) leads to the noise contributions in Eqs. (2), (4) and (5).

Field propagation equations are derived in the paraxial and slowly varying envelope approximations [30]. The former consists in assuming that $|k_{ux}|, |k_{uy}| \ll |k_{uz}| \sim |\mathbf{k}_U|$, where $\mathbf{k}_U = (k_{ux}, k_{uy}, k_{uz})$ is the wave vector of field mode U , whereas the latter prescribes that the spatial and temporal variations of field amplitudes are small, i.e. $|\partial \mathcal{U}^{(\pm)} / \partial z| \ll k_U |\mathcal{U}^{(\pm)}|$ and $|\partial \mathcal{U}^{(\pm)} / \partial t| \ll \omega_U |\mathcal{U}^{(\pm)}|$. Equations (8) and (10) can be written in the form

$$\frac{\partial}{\partial z} \mathcal{U} = L \mathcal{U} + C, \quad (\text{A8})$$

where $L = i\nabla_{\perp}^2 / (2k_U) - \kappa_U / 2$. Propagation due to the operator L is approximated using a second order factorization [39], where the differential operator is evaluated using a two-

dimensional Fourier transform over the transverse directions x, y [40]. There are several options to evaluate the last term of Eq. (A8) [58], but for its simplicity and stability the implicit backward Euler method was chosen. The field at longitudinal point $z + \Delta z$ is thus evaluated as

$$\mathcal{U}(z + \Delta z) = e^{-\frac{\Delta z}{4} \kappa_u(z + \Delta z)} \text{FT}_{xy}^{-1} \left[e^{-\frac{i\Delta z}{2k_u} (k_x^2 + k_y^2)} \text{FT}_{xy} \left[e^{-\frac{\Delta z}{4} \kappa_u(z)} \mathcal{U}(z) \right] \right] + \Delta z C(z + \Delta z), \quad (\text{A9})$$

where FT_{xy} denotes the Fourier transform over transverse directions and k_x, k_y are the associated spatial frequencies. The boundary condition for the pump FEL field at target entrance ($z = 0$) is defined as

$$\mathcal{F}^{(+)}(x, y, z = 0, t) = \frac{\mathcal{F}_0}{q} \exp\left(ik_{\mathcal{F}} \frac{x^2 + y^2}{2q}\right) \exp\left(-\frac{[t - t_0]^2}{4\sigma_{\tau}^2}\right), \quad (\text{A10})$$

where $q = -z_0 - ik_{\mathcal{F}} d_0^2 / (4 \ln 2)$ is the complex beam parameter, $\sigma_{\tau} = \tau_0 / (2\sqrt{2 \ln 2})$, t_0 is a temporal offset, and \mathcal{F}_0 is the normalization constant related to the pump pulse energy E_{FEL} .

Appendix B: Photoionization cross sections

Numerical values of photoionization cross sections for all processes included in the simulation are presented in Table I. Cross sections $\tilde{\sigma}_j$ connected to the dipole matrix elements for resonant excitation to the doubly excited state are calculated using the method of complex rotation [32], and cross sections for ionization of the doubly excited state are calculated using the methods from Refs. [59, 60].

The $n = 3, 4$ excited states of singly ionized helium, which are replaced with a single state $|c\rangle$ in the model, are populated in the following way: ionization of the doubly excited state with the pump and emitted field predominantly populates $\text{He}^+ 3p$ and $4p$ ionic states, whereas ionization of the final state with the pump field mainly produces ions in the $\text{He}^+ 3s$ and $4s$ states. The ratio between the largest and smallest cross section for ionization of these states with a given field is around 3. Since the overall populations of these states are small and hence simulation results are not sensitive to their respective cross sections, we take as $\sigma_{\mathcal{F}c}, \sigma_{\mathcal{E}c}$ the cross sections for photoionization of $\text{He}^+ 4s$, which lie between the values for other states.

Parameter	Value	Parameter	Value
$\tilde{\sigma}_0$	0.044	$\sigma_{\mathcal{F}i}$	1.7×10^{-3}
$\tilde{\sigma}_f$	4.4×10^{-4}	$\sigma_{\mathcal{E}i}$	5.8×10^{-3}
$\sigma_{\mathcal{E}0}$	0.10	$\sigma_{\mathcal{F}b}$	9.8×10^{-4}
$\sigma_{\mathcal{F}f}$	0.032	$\sigma_{\mathcal{E}b}$	4.5×10^{-3}
$\sigma_{\mathcal{F}a}$	0.037	$\sigma_{\mathcal{F}c}$	4.3×10^{-4}
		$\sigma_{\mathcal{E}c}$	1.3×10^{-3}

TABLE I. Values of photoionization cross sections (in atomic units) used in the simulations.

Appendix C: Verification of stochastic noise terms

In the spontaneous emission limit, where the contribution of stochastic terms in Eqs. (2,5) is dominant and stimulated emission is negligible, simulation results can be compared to known analytical solutions. To verify that the electric field produced by the noise terms exhibits the expected characteristics, we consider a simplified three-level system, where photoionization is neglected ($\sigma_{uj} = 0$, $\mathcal{U} = \mathcal{F}, \mathcal{E}$, $j = 0, i, f, a, b, c$) and resonant coupling between the ground and excited state of He^+ is set to zero ($\mu_{ab} = 0$). Additionally, we omit terms proportional to $\mathcal{E}^{(\pm)}$ in the density matrix Eqs. (2,4,5), which produce stimulated emission on the $|i\rangle - |f\rangle$ transition. This allows us to increase the target density without producing amplification of the emitted field, and effectively increase the spontaneous emission signal. This in turn reduces the number of repetitions of the simulation over which the results have to be averaged to obtain convergence [17]. The target pressure of 0.3 mbar is set to be constant throughout the 8 mm long target, and FWHM focus size of the pump pulse with 120 fs duration and 5 μJ pulse energy is set to 10 μm , so that pump pulse divergence inside the target region is negligible.

Under these conditions, the correlation function of the spontaneously emitted field has the discretized form

$$J_{\mathcal{E}}(x, y, z, \tau_1, \tau_2) = \frac{\mathcal{E}_{xyz\tau_1}^{(+)} \mathcal{E}_{xyz\tau_2}^{(-)}}{2\pi\alpha\omega_{\mathcal{E}}} = \frac{2\pi\alpha\omega_{\mathcal{E}} |\tilde{\mu}_{if}|^2 n}{\Delta x \Delta y} \sum_{\tilde{z}=0}^z \Delta z e^{-\frac{\gamma}{2}|\tau_1 - \tau_2|} \rho_{ii,xyz\tau_{\min}} \Theta(|\tau_1 - \tau_2|), \quad (\text{C1})$$

where $\tau_{\min} = \min(\tau_1, \tau_2)$, $\gamma = \Gamma_{if} + 2\Gamma_{if}^D$ is the decoherence rate, and $\Theta(x)$ the Heaviside step function. Due to the properties of stochastic noise terms, field intensity in the spontaneous

emission limit has to be regularized [17], and is calculated as

$$I_{\mathcal{E}}(x, y, z, \tau) = \frac{1}{4} \left(\mathcal{E}_{xyz\tau}^{(+)} \mathcal{E}_{xyz(\tau-\Delta\tau)}^{(-)} + \mathcal{E}_{xyz\tau}^{(+)} \mathcal{E}_{xyz(\tau+\Delta\tau)}^{(-)} + \mathcal{E}_{xyz(\tau-\Delta\tau)}^{(+)} \mathcal{E}_{xyz\tau}^{(-)} + \mathcal{E}_{xyz(\tau+\Delta\tau)}^{(+)} \mathcal{E}_{xyz\tau}^{(-)} \right). \quad (\text{C2})$$

The expected temporal profile of the emitted field intensity can thus be obtained from the field correlation function by setting $\tau_1 = \tau_2 \pm \Delta\tau$. The expected number of emitted photons is

$$N_{\mathcal{E}}^{\text{an.}}(z) = \sum_{xy\tau} \Delta\tau \Delta x \Delta y J_{\mathcal{E}}(x, y, z, \tau, \tau + \Delta\tau) = 2\pi\alpha\omega_{\mathcal{E}} |\tilde{\mu}_{if}|^2 n \Delta\tau \Delta z \sum_{xy\tau} \sum_{\tilde{z}=0}^z \rho_{ii,xy\tilde{z}\tau} e^{-\gamma\Delta\tau/2}. \quad (\text{C3})$$

Since spontaneous emission is a linear process, the intensity of emitted radiation at a given time and position is proportional to the cumulative number of atoms in upper states and the probability for radiative decay, which in Eq. (C1) are encompassed in factors $n\rho_{ii}$ and $2\pi\alpha\omega_{\mathcal{E}} |\tilde{\mu}_{if}|^2 \sim \Gamma_{\text{r}}^f$, respectively, with Γ_{r}^f being the spontaneous radiative decay rate from the doubly excited to the final state. The spectral profile of the emitted field is obtained through the Wiener-Khinchin theorem as the Fourier transform of the time-integrated field correlation function. Exponential factor $\exp(-\frac{\gamma}{2}|\tau_1 - \tau_2|)$ in Eq. (C1) thus reproduces the expected Lorentzian spectral profile of spontaneously emitted fields with width equal to the decoherence rate γ , however, this profile is modified since the upper-state population varies in time. The temporal profile of emitted field intensity thus resembles a convolution of the exponential decay of upper states and temporal dependence of the pumping rate [61]. As shown in Fig. 7(a), the expected spectral profile is slightly wider than the Lorentzian with more rapidly decreasing tails.

Figure 7 presents numerical results averaged over 2×10^5 repetitions of the simulation, along with expected analytical results. The integrated field intensity and spectral intensity at target exit are shown, as well as the number of emitted photons. There is good agreement between numerical and analytical results, with small discrepancies due to averaging over a limited number of repetitions. The imaginary parts of the emitted field intensity and number of photons indicate the level of field fluctuations remaining after averaging, and decrease with increasing number of repetitions.

It is worth noting that a very large number of repetitions is required to obtain approximately smooth average results in the spontaneous emission limit. However, the number of necessary repetitions is drastically reduced when the emitted field starts to amplify and the

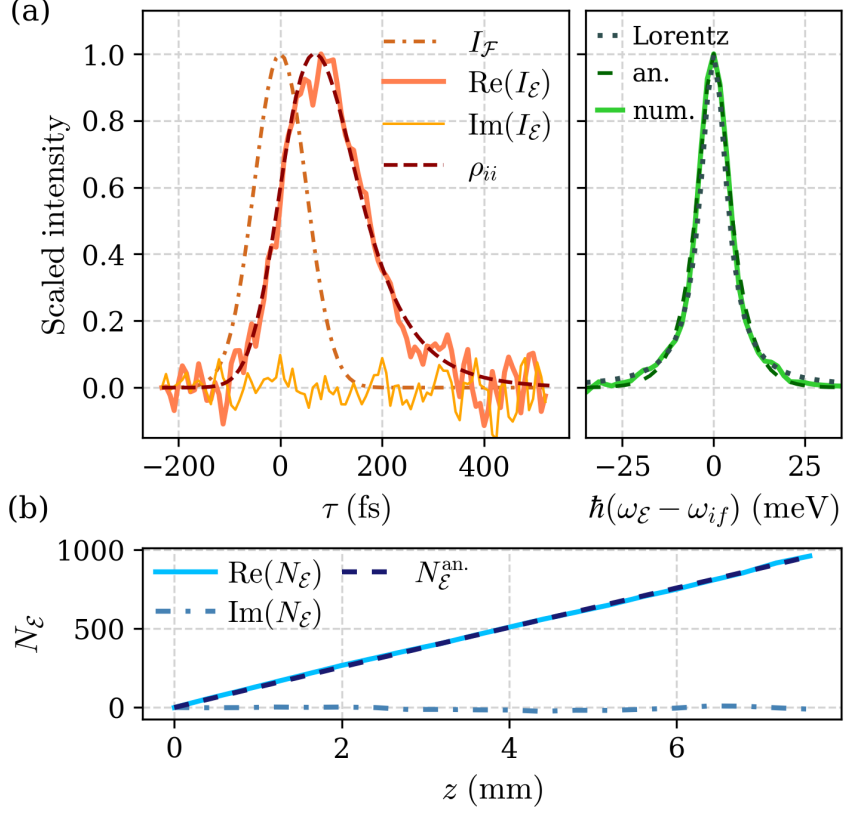


FIG. 7. (a) Left: temporal profile of the pump pulse intensity $I_{\mathcal{F}}$, excited state population ρ_{ii} and emitted field intensity $\text{Re}(I_{\mathcal{E}})$ at target exit integrated over transverse dimensions. Right: spectral intensity of emitted radiation at target exit (num.), along with the expected spectral profile (an.) and Lorentzian profile of width $\gamma = 9$ meV (Lorentz). (b) Numerically and analytically calculated number of emitted photons as a function of propagation distance.

contribution of noise terms becomes less significant. In the spontaneous emission limit, only results averaged over a large ensemble of simulation repetitions can be compared to physical observables, whereas after the initialization of field amplification, individual realizations become relevant and can be related to single-shot experimental results. Since in this paper we are mainly interested in the amplification and saturation regime of superfluorescence, the number of repetitions over which numerical results are averaged can be reduced to a few hundred. Moreover, after amplification the field intensity no longer needs to be regularized, as it coincides with the intensity calculated in the standard way as $I_{\mathcal{E}}(x, y, z, \tau) = \mathcal{E}_{xyz\tau}^{(+)}\mathcal{E}_{xyz\tau}^{(-)}$.